Dalton Transactions

ROYAL SOCIETY OF CHEMISTRY

PAPER

View Article Online
View Journal | View Issue

Cite this: *Dalton Trans.*, 2020, **49**, 3856

Exploring new hydrated delta type vanadium oxides for lithium intercalation†

Joseba Orive, *[a,b] Roberto Fernández de Luis, [c] Edurne S. Larrea, [d] Ana Martínez-Amesti,[e] Angela Altomare,[f] Rosanna Rizzi,[f] Luis Lezama,[d] María I. Arriortua,[c,d] Juan Luis Gómez-Cámer, [g,h] María Jauregui,[h] Montse Casas-Cabanas [h] and Judit Lisoni[b,i]

Received 18th October 2019,
Accepted 10th December 2019

DOI: 10.1039/c9dt04088a

rsc.li/dalton

Three hydrated double layered vanadium oxides, namely $Na_{0.35}V_2O_5{\cdot}0.8(H_2O)$, $K_{0.36}(H_3O)_{0.15}V_2O_5$ and $(NH_4)_{0.37}V_2O_5{\cdot}0.15(H_2O)$, were obtained by using mild hydrothermal conditions. Their delta type structural frameworks were solved by high-resolution synchrotron X-ray powder diffraction and the interlayer spacings were interpreted from difference Fourier maps. The inter-slab distances are modulated by the water content and the special arrangements of the alkali and ammonium cations. The XPS measurements denote mixed valence systems with high contents of V^{4+} ions up to 40%. The monitoring of the V^{4+} EPR signal over time suggests a reduction of the electronic delocalization on account of the partial oxidation to V^{5+}. The electrochemical performance of the active phases is strongly conditioned by the vacuum-drying process of the electrodes, showing better capacity retention when vacuum is not applied. *In situ* X-ray diffraction shows a structural mechanism of contraction/expansion of the bilayers upon lithium insertion/extraction where the alkali ions behave as structural stabilizers. Galvanostatic cycling at very low current density implies migration of the alkali "pillars" triggering the collapse of the structure.

Introduction

The wide variety of vanadium oxidation states, 3+, 4+ and 5+, confers great versatility to adopt different coordination environments.[1] The polymerization of VO_n chains to form layers and frameworks through edge and corner-sharing of vanadium oxide units leads to a broad range of architectures adequate for reversible lithium insertion/extraction.[2] In fact, vanadium-based compounds such as V_2O_5, $VO_2(B)$, LiV_3O_8, and $Li_3V_2(PO_4)_3$ have generated great interest as intercalation-electrode materials for lithium-ion batteries (LIBs).[3,4]

The V–O phase diagram[5] represents a complex system constituted by the so-called Magneli (V_nO_{2n-1}) and Wadsley ($V_{2n}O_{5n-2}$) phases, which differ in the width of their homogeneity ranges and the concentrations of oxygen and vanadium vacancies.[6] While rutile type Magneli phases have inspired the development of electronic devices through insulator to metal transitions and anisotropic charge transport properties,[7,8] the layered Wadsley phases allow reversible ion intercalation.[9]

Many studies point to the improvement in lithium diffusion and electrical conduction performance by the addition of alkaline-earth metal ions[10] or ammonium ions[11–13] into the V_2O_5 host or other vanadium oxide-based matrices. Following this approach, it is possible to increase the interlayer space and stabilize the structure during lithium insertion/extraction.[14,15]

Vanadium oxide bronzes of the general formula $M_xV_2O_5$ can be classified into single layered- and double layered structures.[16] While the single layered phases retain the V_2O_5 crystal structure composed of VO_5 square pyramids sharing oxygen vertices, the double layered- or delta-type structures are constituted by condensed V_4O_{10} double layers made up of edge-sharing distorted VO_6 octahedra. The $M_xV_2O_5$ bronzes rep-

[a]Dpto. de Ingeniería Química, Biotecnología y Materiales, FCFM, Universidad de Chile, Av. Beauchef 851, Santiago 8370448, Chile. E-mail: joseba.orive@ing.uchile.cl
[b]NM MultiMat, Chilean Ministry of Economy, Development and Tourism, Chile
[c]BCMaterials (Basque Centre for Materials, Applications & Nanostructures), Bld. Martina Casiano, 3rd. Floor UPV/EHU Science Park, Barrio Sarriena s/n, 48940 Leioa, Spain
[d]Dpto. de Mineralogía y Petrología and Dpto. de Química Inorgánica, Facultad de Ciencia y Tecnología, Universidad del País Vasco UPV/EHU, Sarriena s/n, 48940 Leioa, Spain
[e]SGIker, Servicios Generales de Investigación UPV/EHU, Avda. Tolosa 72, 20018 Donostia-San Sebastian, Spain
[f]Institute of Crystallography-CNR, via Amendola 122/o, Bari, Italy
[g]Dpto. de Química Inorgánica e Ingeniería Química, Universidad de Córdoba, 14071 Córdoba, Spain
[h]CIC Energigune, Parque Tecnológico de Álava, Albert Einstein 48, 01510 Miñano, Spain
[i]Instituto de Ciencias Físicas y Matemáticas, Facultad de Ciencias, Universidad Austral de Chile, Valdivia, Chile

†Electronic supplementary information (ESI) available. See DOI: 10.1039/C9DT04088A

resent flexible systems that can interchange ions with a huge variety of ionic radii and valences (Li^+, Na^+, K^+, Cu^+, Ag^+, Mg^{2+}, Ca^{2+}, Sr^{2+}, Ni^{2+}, Mn^{2+}, and Fe^{2+}) with possible electronic alterations but without great geometric distortions of the mother structures.[17] The vast possibilities of tuning these kinds of compounds by modifying the space between the vanadium oxide layers with different coordination environments together with the ability to accommodate V^{4+}/V^{5+} mixed-valence states, vacancies and nonstoichometry[18] make them interesting cathode archetypes for LIBs.

Moreover, crystalline δ-phase vanadium oxides extensively studied for lithium intercalation by Whittingham's group[2,4,19] are recently receiving renewed interest as multivalent-ion battery materials, where their maximum exponent, the $NH_4V_4O_{10}$ phase, shows great versatility as a cathodic material for both monovalent Li[20–23] and Na[24–27] and divalent batteries, such as Mg,[28,29] Zn[30,31] and Ca[32] ones. Furthermore, interlayer engineering by hydrated intercalation species has been shown to be an effective strategy to improve the structural stability during charge–discharge processes and provide fast ion diffusion paths in zinc-ion storage systems.[33–35]

With the aim of identifying new inspiring host materials, the present work discloses the preparation of a series of delta type vanadium oxides with the interlayer spacing modulated by the water and the alkali content. The structural frameworks were solved by high-resolution synchrotron X-ray powder diffraction and the electrochemical properties were described and discussed by considering the role of water and alkali "pillars" in the structures. We will show how the vacuum-drying process of the electrodes, foreseen to control the stacking disorder degree within the vanadium oxide layers, affects the capacity retention of the studied compounds.

Experimental section

Synthesis and characterization

$Na_{0.35}V_2O_5{\cdot}0.8(H_2O)$ (**$NaVO_x$**), $K_{0.36}(H_3O)_{0.15}V_2O_5$ (**KVO_x**) and $(NH_4)_{0.37}V_2O_5{\cdot}0.15(H_2O)$ (**$NHVO_x$**) phases were prepared using mild hydrothermal conditions under autogenous pressure. A water solution of $VOSO_4$ (0.75 mmol) was acidified with H_2SO_4 (1.4 mmol for **$NHVO_x$** and 2 mmol for **$NaVO_x$** and **KVO_x**) and $H_2C_2O_4{\cdot}2H_2O$ (0.75 mmol). The mixtures continuously stirred in air were basified to increase the pH by adding dropwise 2 M NaOH and 2 M KOH solutions for **$NaVO_x$** (pH = 4.5) and **KVO_x** (pH = 4.5) and NH_4OH solution (25% NH_3 in H_2O) for **$NHVO_x$** (pH = 2.5). The resulting solutions (total volume = 30 ml) were sealed in a 35 ml PTFE-lined stainless-steel pressure vessel (fill factor 85%). After 48 hours for **$NHVO_x$** and 60 hours for **$NaVO_x$** and **KVO_x** at 160 °C, fine-grained bluish-black powders were recovered and washed with water and acetone. Attempts to obtain single crystals were not successful. The absence of H_2SO_4 or $H_2C_2O_4{\cdot}2H_2O$ in the hydrothermal system results in the crystallization of the monoclinic VO_2(B) polymorph (PDF file: 01-081-2392; S.G. *C*2/*m* (12), a = 12.093 Å, b = 3.702 Å, c = 6.433 Å, β = 106.97°).[36]

Vanadium, potassium and sodium contents were confirmed by inductively coupled plasma quadrupole mass spectrometry (ICP-Q-MS) analysis, performed with a Thermo Scientific XSERIES 2 spectrometer. The amount of N in **$NHVO_x$** was determined by elemental analysis (see Table S1†). The samples were also characterized by powder X-ray diffraction. The patterns were recorded on a Bruker D8 Advance diffractometer (CuKα radiation) (2θ range = 5–80°, step size = 0.02°, exposure time = 0.3 s per step).

Scanning electron microscopy

The microstructure and composition were studied using a JEOL JSM-7000F scanning electron microscope (SEM) equipped with a Schottky field emission gun (FEG) and an Oxford Inca Pentafet X3 energy dispersive X-ray analyser (EDX). The EDX microanalysis was performed using an accelerating voltage of 20 kV and a current intensity of 1×10^{-10} A, with a working distance of 10 mm.

High-resolution synchrotron X-ray powder diffraction

The X-ray patterns of **$NHVO_x$**, **$NaVO_x$** and **KVO_x** were collected in transmission configuration on the BM25B SpLine of the European Synchrotron Radiation Facility (ESRF) at room temperature. The powder samples were loaded in glass capillaries (∅ = 0.5 mm) and rotated during data collection to enhance particle statistics. The wavelength was set at 0.62097 Å (20 keV) and the patterns were recorded with the following characteristics:

- **$NHVO_x$**: 2–47.1°, 0.01°, 6 s per step.
- **$NaVO_x$**, **$NaVO_x$_HT** and **KVO_x**: 2–26.1°, 0.0125°, 3 s per step; 26.1°–47.1°, 0.0125°, 4 s per step.

Thermal induced structural change due to the partial dehydration of **$NaVO_x$** was followed by heating the capillary using a hot-air blower up to 110 °C (**$NaVO_x$_HT**).

Indexing process, space group determination and *ab initio* structural solutions were performed with the EXPO2014 program.[37] There was the possibility of finding the positions of the vanadium and oxygen atoms of the inorganic frameworks of **$NaVO_x$**, **KVO_x** and **$NHVO_x$**. The extraframework species located in the interlayer spaces were tentatively assigned in a first approach.

Le Bail and Rietveld refinements were addressed using the FullProf program.[38] The instrumental contribution to peak broadening was determined with a LaB_6 standard. The resulting instrumental resolution function was included in the refinement, although U, X, and Y of the pseudo-Voigt profile function of Thompson, Cox and Hastings[39] were allowed to vary in the refinement. First of all, the profile variables such as the zero shift offset, profile parameters, lattice constants, asymmetry parameters, and background were cyclically refined. Anisotropic line broadening was detected and modeled with FullProf as a linear combination of spherical harmonics, where the anisotropic size is supposed to contribute to the Lorentzian component of the total Voigt function.[40] The most important contribution to this effect is believed to be due to the platelet shape of the compounds (Fig. 1),

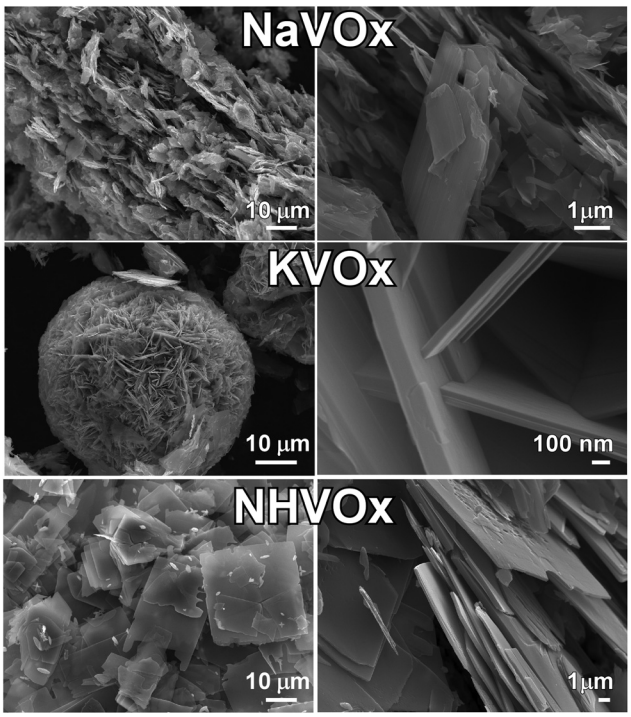

Fig. 1 FEG-SEM of the $NaVO_x$, KVO_x and $NHVO_x$ samples.

although stacking disorders along [001] as previously observed in other laminar phases[41] cannot be discarded. The samples were successfully refined using the *C*2/*m* space group, resulting in the unit cell parameters shown in Fig. 2(a) (see also Table S2†). The good agreement between the experimental and the calculated diffractograms confirms the purity of the samples. An additional spurious peak at 9.53° (2θ) in KVO_x was detected in the synchrotron measurement (asterisk in the inset of KVO_x refinement) and discarded as a reflection of the phase by comparison with the laboratory diffractometer data of a previous analysis of the same sample (Fig. S1†). Fig. S1† also shows that the effect of preferred orientation of the 00l family of reflections is highly minimized when the sample is measured in transmission mode.

For Rietveld refinements (Fig. S2 and Tables S2–S4†), an overall thermal parameter was considered in all phases except in $NaVO_x$, where it was possible to refine three independent isotropic displacement parameters, distinguishing the vanadium atoms, the oxygen atoms and the host ions. Some V–O constraints were included to maintain a stable and chemically correct structural model during refinement of the atomic coordinates. Once the inorganic frameworks were refined, difference Fourier maps using F_{obs}–F_{calc} values were constructed in order to locate the interlaminar species.

Physicochemical characterization techniques

Thermogravimetric analysis was performed under a nitrogen atmosphere using a Netzsch STA 449 F3 Jupiter simultaneous TG-DSC thermo-microbalance. An alumina crucible containing around 10 mg of the sample was heated in N_2 at a rate of 5 °C min^{-1} from room temperature to 800 °C. Thermodiffractometric experiments were carried out in air using a Bruker D8 Advance diffractometer (Cu Kα) equipped with a variable-temperature stage (HTK2000), a Pt sample heater and a Vantec high-speed one dimensional detector with six degrees of angular aperture. The powder patterns were

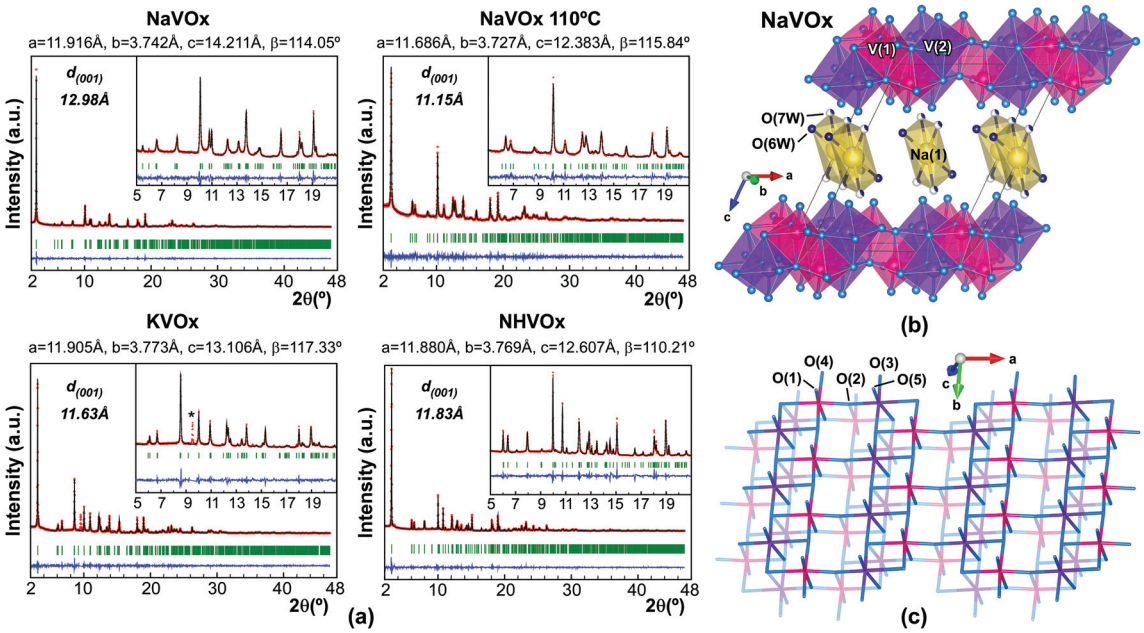

Fig. 2 (a) Observed (red dots), calculated (black lines) and difference X-ray powder diffraction patterns (blue lines) for the Le Bail analysis of the phases. (b) Polyhedral representation showing the interlaminar space and (c) scheme of the double layered structure of $NaVO_x$. Color code: $V(1)O_6$ octahedra, pink; $V(2)O_6$ octahedra, purple; oxygen, blue; sodium, yellow.

recorded in the $5 \leq 2\theta \leq 38°$ range (step size = 0.033° and time per step = 0.5 s) at intervals of 15 °C, increasing the temperature at 10 °C min^{-1} from room temperature to 810 °C. The IR spectrum (KBr pellet) was obtained using a Bruker Vector 22 spectrophotometer in the 400–4000 cm^{-1} range. Raman spectra were recorded on a Renishaw Raman confocal microscopy spectrophotometer using the 514 nm laser line for excitation. X-ray photoelectron spectra were obtained using a Specs (Berlin, Germany) system equipped with a Phoibos 150 1D-DLD analyzer, monochromatic AlKα radiation (1486.6 eV, 300 W, 13 kV) source and multi-channel detector. Spectra were recorded in the constant pass energy mode at 80 eV for survey spectra and 30 eV for high resolution spectra, with an electron take-off angle of 90°. The spectrometer was previously calibrated using the Ag $3d_{5/2}$ line at 368.26 eV. The binding energy of adventitious carbon (C 1s) was set at 284.6 eV to correct sample charging. The spectra were fitted with the CasaXPS 2.3.16 software that models the Gauss–Lorentzian contributions, after background subtraction (Shirley). X-band EPR measurements were carried out using a Bruker ELEXSYS 500 spectrometer equipped with a super-high-Q resonator ER-4123-SHQ, a maximum available microwave power of 200 mW and standard Oxford Instruments low temperature devices. Samples were placed in quartz tubes and the spectra were recorded at different temperatures between 5 and 300 K using a modulation amplitude of 0.1 mT at a frequency of 100 kHz. The magnetic field was calibrated by an NMR probe and the frequency inside the cavity (~9.4 GHz) was determined with an integrated MW-frequency counter.

Electrochemical measurements

The electrodes were prepared by casting a slurry of a mixture of the vanadium oxides, conductive agent (carbon Timcal C45), and binder (5 wt% solution of polyvinylidene fluoride dissolved in *N*-methyl pyrrolidone) onto a carbon-coated Al-foil in a 70 : 15 : 15 mass ratio, respectively. The electrodes were dried at 100 °C for 12 h under vacuum (*_vac*) or without vacuum (*_novac*) and were then cut (∅ = 11 mm), pressed and transferred to an Ar-filled glovebox with water and oxygen levels below 0.1 ppm. The electrodes dried under vacuum had loadings around 1 mg and those dried without vacuum between 2.28 and 4.40 mg. Swagelok type cells were assembled against a lithium metal foil. The electrolyte consists of 1 M $LiPF_6$ dissolved in 1 : 1 v/v ethylene carbonate/dimethyl carbonate (EC/DMC) solvent impregnated on a Whatman GF/D porous glass fiber separator. Electrochemical evaluation of the samples was made at room temperature in a Maccor Battery Tester and a BioLogic VMP3 Multichannel potentiostat-galvanostat. Cyclic voltammetries with 4 cycles for every scan rate were run, increasing from 0.1 mV s^{-1} to 0.5 mV s^{-1} and then to 1.0 mV s^{-1} in the voltage range of 1.5–4.5 V. Rate capability measurements comprising repeated cycling at 15, 30, 75, 150, 300 and 600 mA g^{-1} were made. Electrochemical impedance spectroscopy measurements were performed using a three-electrode configuration test cell (EL-CELL) with a lithium reference ring from 100 kHz to 5 mHz.

To uncover the structural mechanism upon electrochemical cycling, *in situ* X-ray diffraction (XRD) coupled to electrochemical galvanostatic (GCPL) measurement was carried out. For XRD measurement, a Bruker D8 Advance X-ray diffractometer with CoKα radiation and equipped with a LYNXEYE detector was used. For the electrochemical experiment, a home-made electrochemical cell was used. This electrochemical cell with 18 mm inner diameter and equipped with a Be window as a current collector was operated in reflection geometry in order to obtain a correlative picture of the phase transformation occurring upon cycling and to ascertain its impact on electrochemical properties. Each XRD scan was collected every 0.05° between 15° and 55° (2θ). The active material was prepared by mixing $\mathbf{KVO_x}$ with carbon (Ketjen Black EC-600JD, Akzo Nobel) in a ratio of 80 : 20. About 114 mg of this mixture were placed in the cell against the Be window, below a Whatman GF/D separator impregnated with 1 M $LiPF_6$ in EC : DMC (1 : 1 vol%) and lithium metal foil as the anode. The cell was galvanostatically cycled at a current density of 6.0 mA g^{-1}.

Results and discussion

Morphology and structure description

FEG-SEM micrographs reveal different crystal morphologies of the compounds (Fig. 1). $\mathbf{NaVO_x}$ is constituted by brittle sheet crystals, $\mathbf{NHVO_x}$ exhibits square-shaped micrometric sheet crystals and $\mathbf{KVO_x}$ is formed by microspheres assembled of laminar crystals of nanometric thickness (from 100 to 200 nm).

The inorganic framework of the laminar vanadium oxides consists of V_2O_5 bilayers forming infinite 2D $[V_4O_{10}]_n$ sheets separated by intercalated cations and water molecules (Fig. 2b) inducing partial reduction to V^{4+}. The coordination environment of the two crystallographically independent V atoms has been solved as distorted octahedra that share edges to define double chains running parallel to [010], which arrange side by side by interchain V–O(2) bonds through sharing the corners of octahedra to form the slab (Fig. 2c). The interlayer *d* spacing, corresponding to the most intense diffraction peak at $2\theta \sim 3°$ from the (001) facet, is calculated to be 12.98, 11.15, 11.83 and 11.15 Å for $\mathbf{NaVO_x}$, $\mathbf{NaVO_x}$**_HT**, $\mathbf{NHVO_x}$ and $\mathbf{KVO_x}$ respectively. Because the alkali content is almost the same in the phases, ranging from 0.35 to 0.37 atoms per formula unit, it could be claimed that the peak position change suggests that the interlayer expansion is mainly governed by the intercalated water.

Taking into account the difference Fourier maps (F_{obs}–F_{calc}), characteristic electron density patterns can be observed for each of the phases that suggest unique arrangements of the host ions (Fig. 3). For $\mathbf{NaVO_x}$, an electron density with sigmoidal shape is located in the center of the unit cell, suggesting a disorder around a special position. However, the Fourier map shows an electron density peak in the special position that is assigned to a sodium atom whose occupation factor is allowed to vary reaching a value of 0.24(1), close to the chemical occupation inferred from the ICP analysis, 0.175. Two more electron densities located in general positions

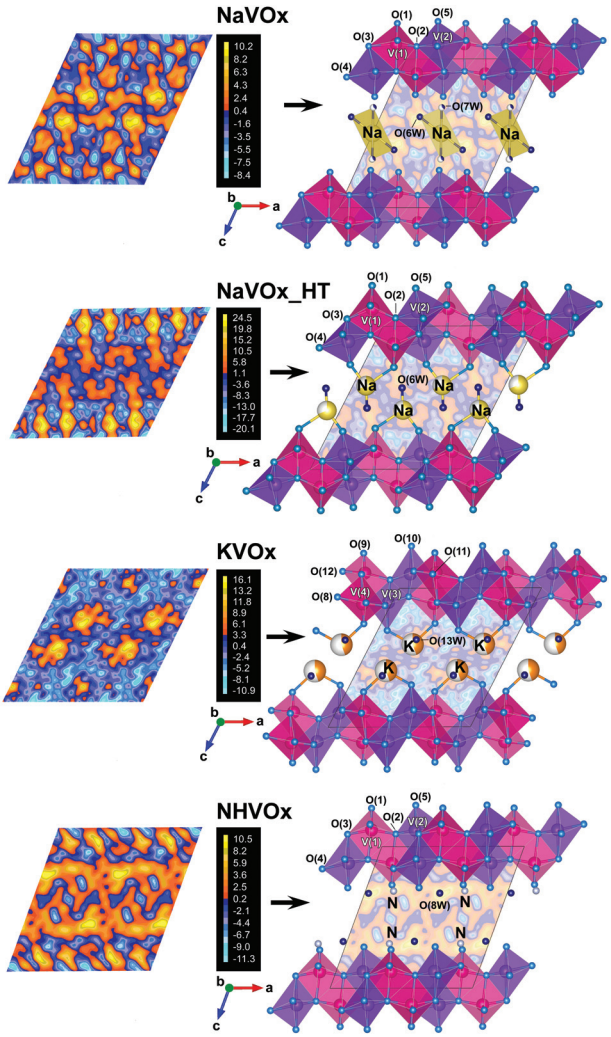

Fig. 3 Fourier maps of $F_{obs}-F_{calc}$ differences and interpretation of the interlaminar electronic densities in the four phases.

around the sodium atom were attributed to the water molecules O(6W) and O(7W) giving rise to a trigonal prismatic geometry (Fig. 2b). When **NaVO$_x$** is heated to 110 °C (**NaVO$_x$_HT**), the sodium atom is delocalized in the two general positions. As a consequence, the O(7W) water molecule leaves the structure by shortening the *c* parameter, while the other electron density attributed to the O(6W) water molecule loses intensity with respect to its homologue at room temperature in agreement with the thermogravimetric analysis. With respect to **KVO$_x$**, a well located maximum in the general position is observed and is attributed to the potassium atom. In the case of **NHVO$_x$**, a continuous electron cloud attached to the inorganic framework is observed, suggesting disorder between ammonium ions and water molecules. However, some more intense maxima are distinguished within the electron cloud, which were attributed to the nitrogen and oxygen atoms corresponding to the ammonium ion and the water molecule, respectively.

To the best of our knowledge, since the pioneering studies of Oka[42–45] and Whittingham[46] on the hydrothermal synthesis of alkali-containing hydrated vanadium oxides, we have not found any reports describing the title compounds. In particular, we have not found compounds combining *d* spacings and β angle values above 11 Å and 110°, respectively. Similar archetypes such as $[N(CH_3)_4]_zM_yV_2O_5{\cdot}nH_2O$ (M = Fe,[47] Mn[48]) display monoclinic structures with β angles of 107° and 109° and $d_{(001)}$ around 13 Å, where tetramethyl ammonium and M^{2+} ions are suggested to reside in a disordered manner between the oxide sheets. $M_{0.25}V_2O_5{\cdot}H_2O$ (M = Ca, Ni) compounds solved by single crystal X-ray diffraction[49] exhibit interlayer Ca and Ni atoms located in the 4i and 2c positions, respectively. The neighboring Ca sites are too close (around 1 Å) to be occupied simultaneously. Such difference in the location of the interlayer ions seems to have a direct impact on the β angles of the unit cell, being 95° in the Ni compound and 105° in the Ca analogue.

In our case, the β angles are greater than 110° and therefore a greater shear of the oxide sheets could suggest a possible disorder of the interlaminar species. We have tried to offer a general overview of the structures whose inorganic buildings have been solved by using *ab initio* calculations. The interlaminar electronic densities were interpreted from their Fourier maps, but being aware of the location of the specific positions of those light weight extra-framework species remains a challenge. In addition, with the current powder diffraction data, the effects of the anisotropic line broadening and preferred orientation, mainly due to the crystal morphology, hinder the structure refinement.

Thermal and spectroscopic study

Thermodiffractometric (TDX) experiments disclose the thermal stability of the phases which suffer structural transformations due to the interlayer water content release, which is found to be very different in the three phases according to the thermogravimetric curves (Fig. 4a). In the case of **NaVO$_x$**, the atomic reorganization is very sudden at 90 °C (Fig. 4b) and coincident with the first thermal decomposition observed in the thermogravimetric curve (30–90 °C), which can ascribed to the loss of $(H_2O)_{0.57}$ per formula unit. The structure of this dehydrated phase (**NaVO$_x$_HT**) collapses at 250 °C probably due to the loss of more strongly hydrogen-bonded water molecules [90–360 °C, $(H_2O)_{0.23}$]. For **NHVO$_x$**, a continuous weight loss of 5.5% up to 430 °C is observed and attributed to the release of the water content [30–200 °C, $(H_2O)_{0.15}$] and the ammonium ions [200–430 °C, $(NH_4)_{0.37}$]. The water content release triggers the progressive destruction of the crystalline framework of **NHVO$_x$**, which is stable up to 210 °C (Fig. 4c) after which the most intense (001) reflection starts to decrease in intensity and shifts to higher 2θ angles due to the interlayer space collapse. The crystallization of an ammonium containing a dehydrated phase with smaller interlayer space also occurs, coexisting with **NHVO$_x$** up to 360 °C. From this temperature, the ammonium ions release from the second phase and the V_2O_5 (*Pmmn*) phase crystallizes as a decomposition product. **KVO$_x$** displays the lowest mass loss, being 1.5% at 360 °C, and is attributed to the presence of more strongly bound water mole-

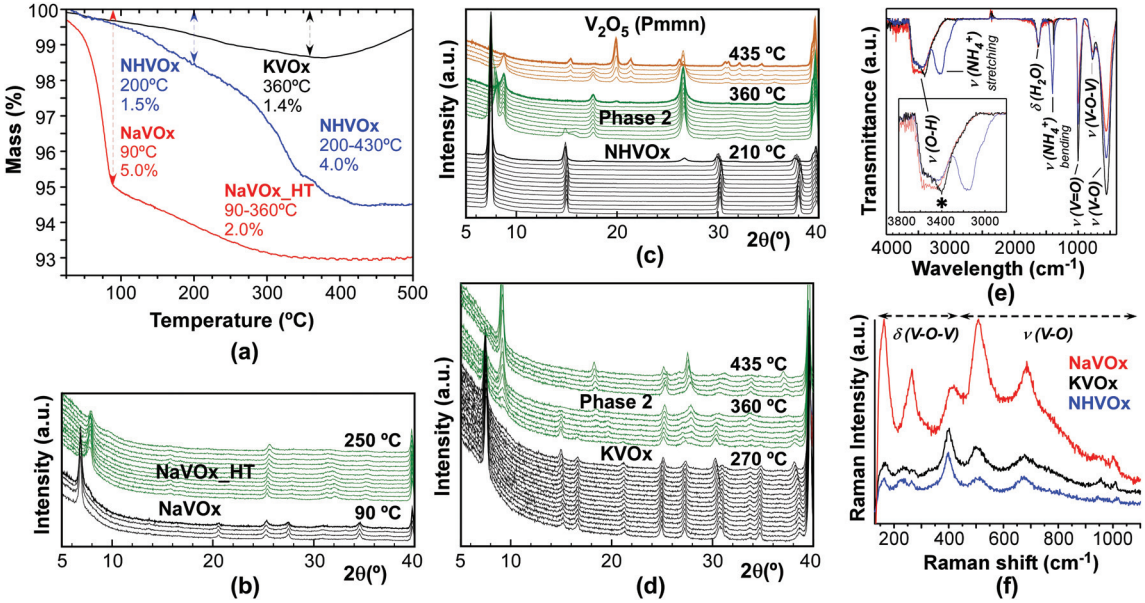

Fig. 4 (a) Thermogravimetric curves. Thermodiffractograms of (b) **NaVO$_x$**, (c) **NHVO$_x$** and (d) **KVO$_x$**. (e) IR and (f) Raman spectra.

cules that could be considered protonated as has been suggested in $V_2O_5{\cdot}nH_2O$ xerogels.[50] The stronger character of the interlayer water is also reflected in a greater thermal stability of its crystal structure which shows no major changes up to 270 °C (Fig. 4d). Here, the phase begins to break down and a potassium containing phase with a smaller interlayer space also crystallizes, coexisting together until 360 °C. This phase could not be isolated by thermal treatments in order to be characterized but its thermal evolution was followed as a single phase from 375 °C to 435 °C and a diffraction pattern was measured at 380 °C. Starting from the unit cell parameters of **KVO$_x$**, a pattern matching of the high temperature phase was performed in the same space group *C*2/*m*, obtaining the following unit cell parameters: a = 12.032(3) Å, b = 3.634(2) Å, c = 10.974(3) Å, and β = 94.69(2)°. An expected decrease of the parameter c is observed together with a drastic change in the beta angle which is reminiscent of the angles found in vanadium oxide xerogels.[51,52]

The IR spectra of the compounds present the distinctive vibrational modes of other similar vanadium oxide networks as the double layered $V_2O_5{\cdot}nH_2O$[53] xerogels and the intercalated $M_xV_2O_5{\cdot}nH_2O$[54] structures. The strongest bands, centered at 560 cm^{-1}, are related to the edge-sharing V–O stretching vibrations, the bands located at 775 cm^{-1} are attributed to the asymmetric stretching vibration modes of V–O–V links and the sharp bands at 1000 cm^{-1} are attributed to the stretching vibrations of the terminal V═O groups pointing to the interlayer spaces. The bands at 3160 and 1402 cm^{-1} are, respectively, attributed to the asymmetric stretching and the symmetric bending vibrations of NH_4^+ groups as host ions in the interlayer space of **NHVO$_x$**. The bands at around 3500 and 1625 cm^{-1} correspond to the stretching and bending vibrations of water molecules. The highest frequency band is wide and not well resolved. However, in **KVO$_x$**, a distinctive feature can be observed; the band seems to unfold in a more intense band located around 3400 cm^{-1} (denoted by an asterisk in the inset of IR spectra of Fig. 4e). It is known that the increased strength of hydrogen-bonding typically shifts the stretch vibration to lower frequencies (red-shift). So, we have concluded that the water molecules in **KVO$_x$** are protonated, H_3O^+, in accordance with their greater thermal stability observed in the TGA.

The Raman spectra of the compounds (Fig. 4f) exhibit broad bands which have been compared and interpreted on the basis of the fingerprint of a delta type potassium compound, $K_{0.5}V_2O_5$,[55,56] which in turn, despite the difference in their symmetry, took into account the V–O covalent network of the V_2O_5 orthorhombic structure (Table S5†). Phonon modes below 400 cm^{-1} are the product of the V–O bond bending vibrations, while the higher-frequency modes are due to the stretching vibrations. The high intensity of the Raman line (signals B_{1g} and B_{3g}) usually observed in V_2O_5 compounds located around 145 cm^{-1} is correlated with the long-range order in the V–O layers.[57] The introduction of host ions into the interlayer spaces results in a shift of the band to higher wavelengths (166 cm^{-1}) as previously observed in $K_{0.5}V_2O_5$ and the studied compounds. The very low intensity of the translational mode in **KVO$_x$** and **NHVO$_x$** could indicate local disorder in the vanadium oxygen layers of the compounds. Unlike the strong bands found in $K_{0.5}V_2O_5$ at 784 and 887 cm^{-1}, the title compounds do not show Raman signals in this region as is also observed in the α-V_2O_5 structure. The antisymmetric stretching modes of the V–O–V bridges that are Raman active in this region are not visible because of their linear character.[58] When the power was increased to 50% of the incident laser beam some *in situ* phase transitions were observed. The

bands corresponding to the translational modes gain intensity, mainly in **KVO$_x$** and **NHVO$_x$**, and suffer significant shifts to lower wavelengths in case of **NaVO$_x$** and **NHVO$_x$**, from 166 cm^{-1} to 148 cm^{-1} and to 143 cm^{-1}, respectively (Fig. S3†). This mode in **KVO$_x$** does not undergo any shift that fits with a greater stability of its delta type structure unlike what was observed for **NHVO$_x$** and **NaVO$_x$** which seem to be degraded to V_2O_5.

X-ray photoelectron spectroscopy (XPS) was performed to assess the chemical composition and the charge state of the vanadium of the title phases. The correct intercalation of the corresponding host ions in the interlayer spaces was confirmed by the signals belonging to N 1s (401.8 eV), K 2p (292.8 and 295.6 eV) and Na 1s (1071.7 eV) (Fig. 5). The high resolution XPS spectra of V 2p display the V 2p$_{3/2}$ peak with the broader signal of the V 2p$_{1/2}$ spin–orbit pair located at a higher binding energy (~7 eV) (Fig. 5). The V 2p$_{3/2}$ core peak can be deconvoluted into two components, V 2p$_{3/2}$(IV) (**NHVO$_x$**: 516.3 eV, **KVO$_x$**: 516.2 eV and **NaVO$_x$**: 516.4 eV) and V 2p$_{3/2}$(V) (**NHVO$_x$**: 517.7 eV, **KVO$_x$**: 517.6 eV and **NaVO$_x$**: 517.8 eV), denoting the coexistence of the V^{5+}/V^{4+} redox couple in the vanadium oxide bronzes.

The peak area integration of the V 2p$_{3/2}$ signals determines the V^{5+}/V^{4+} ratio, being 1.40 : 1, 1.57 : 1 and 2.40 : 1 in the **NHVO$_x$**, **KVO$_x$** and **NaVO$_x$** phases, respectively. The V^{4+} content determined by XPS is much higher in the studied compounds than those observed in other delta type structures such as the $NH_4V_4O_{10}$ compound where the V^{5+}/V^{4+} ratios were found to be around 3 : 1.[26,27,32]

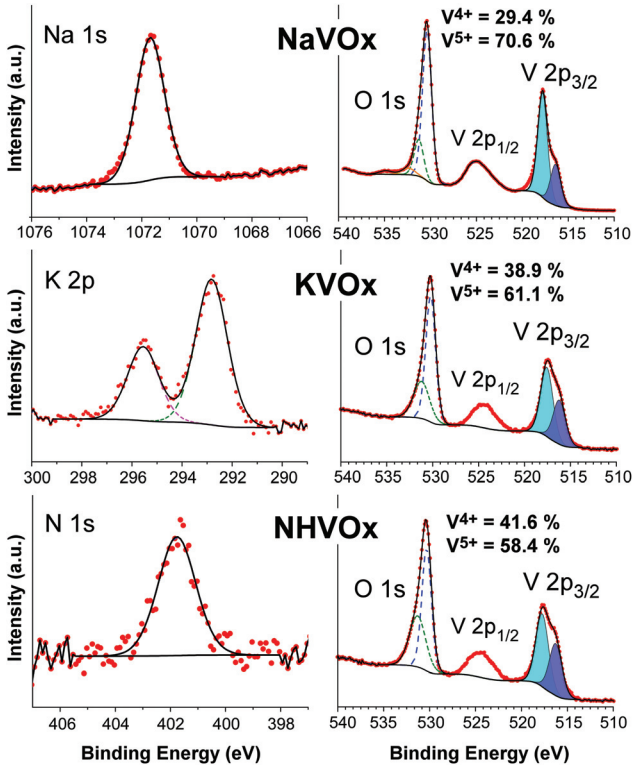

Fig. 5 XPS spectra of **NaVO$_x$**, **KVO$_x$** and **NHVO$_x$**.

Doping on the vanadium site of $NH_4V_4O_{10}$ has been proved to be a good strategy to increase the V^{4+} proportion,[27,32] resulting in a V^{5+}/V^{4+} ratio of 2.33 : 1 in a Na-doped structure. The authors observed a shift of the O 1s peak to higher binding energies which is explained by the creation of oxygen vacancies. The existence of V^{4+} proportions as high as 40% in the **KVO$_x$** and **NHVO$_x$** surfaces, never before reported in delta type structures, is probably a consequence of combining a V^{4+} source ($VOSO_4$) in the presence of a reducing agent such as oxalic acid, which prevents total oxidation to V^{5+} during the hydrothermal process giving rise to mixed valence systems.

The peaks at binding energies of around 530.3 and 531.3 eV are attributed to the O 1s orbitals of the O–V^{5+} and O–V^{4+} bonds, respectively, whose ratios are in good agreement with the V^{5+}/V^{4+} ratios estimated from the deconvolution of the V 2p$_{3/2}$ signals. **NaVO$_x$** displays two small additional signals at 532.4 and 534.9 eV. The first one could be attributed to the interlayer H_2O molecules weakly linked to the inorganic building that start to release close to room temperature and cause the structural transformation to **NaVO$_x$_HT** at 90 °C, as was observed in the TGA and TDX. The latter signal probably comes from the adsorbed moisture over the surface.

The EPR spectra of the freshly prepared samples only show very weak signals at room temperature in the three compounds, although the smaller linewidth in the case of **NHVO$_x$** favors its detection. In the samples kept in capillary tubes open to the atmosphere, it can be observed that the intensity of the signals increases slowly but significantly with time, while their linewidths are reduced (Fig. 6).

After six months, resonances with the shape of the derivative of the Lorentzian function were easily detected, being 24.8, 18.4 and 13.0 mT for the peak-to-peak linewidths of the Na, K and NH_4 compounds, respectively. The center of the resonances gives a similar g value of 1.96 for all cases, which is in good agreement with the g values reported for V^{4+} centers in other vanadium pentoxide derivatives.[59,60] As the temperature was lowered, a strong increase in the EPR signal intensity was observed. Besides, some peaks from a hyperfine structure due to the coupling of the electronic moment of the unpaired V^{4+} electron with the magnetic moment of the ^{51}V nucleus (I = 7/23) could be detected (Fig. S4†). From the magnetic field separation between neighboring peaks in the splitting, the parallel hyperfine coupling constant could be deduced for the NH_4 compound: A_{II} = 20.1 mT (g_{II} = 1.939). Actually, the observed low temperature spectra correspond to the superposition of a weak structured signal arising from isolated V^{4+} ions and a broader resonance line, resulting from exchange coupled V^{4+} ions in magnetically non-equivalent sites. A similar behaviour has been previously observed in vanadium pentoxide gels[61] or vanadium oxide nanotubes.[62]

Electrochemical study

Four successive cyclic voltammetry (CV) curves in the voltage range from 1.5 to 4.5 V were first measured at a sweep rate of 0.1 mV s^{-1} to investigate Li ion insertion and deinsertion behavior depending on the vacuum effect on the drying treat-

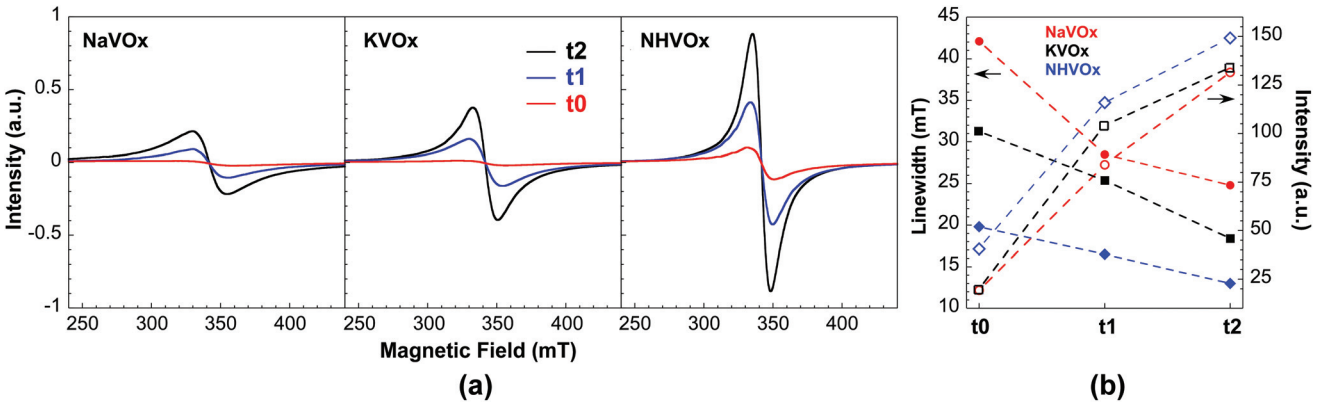

Fig. 6 (a) X-band EPR powder spectra measured at different times (*t*1 = as-synthesized, *t*2 = after 1 month, *t*3 = after 6 months) for the three compounds. (b) Time evolution of the linewidth and intensity of the EPR signals of the compounds.

ment of the electrodes. A cathodic scan (reduction process) is first performed, followed by an anodic scan (oxidation process). Electrodes dried under vacuum (*_vac*) display 2 main cathodic peaks at around 2.47 V and 2.34 V, respectively, in the first cycle (see the insets of Fig S5† for more detailed potential values). **NaVO$_x$_HT_*vac*** and **KVO$_x$_*vac*** undergo a shift of 20–40 mV to smaller potentials with the successive cycling up to the fourth cycle and to higher potentials in the case of **NHVO$_x$_*vac***. A significant decrease of the 2.47 V peak area is also observed, suggesting capacity fading. In contrast, when the vacuum is not applied (*_novac*), after the initial activation cycle (the insets of Fig S5†), the peak positions and areas remain almost invariant in the subsequent CV curves, demonstrating excellent electrochemical reversibility and superior cycling stability.

As the scan rate is increased up to 0.5 mV s^{-1} and then to 1 mV s^{-1}, there is evidence of surface layer formation, deduced from the greater current area in the first cycle compared with the subsequent cycles.[63] In addition, increasing the scan rate enables better identification of the redox pairs at higher voltages, mainly visible in the *_vac* samples. The cathodic–anodic couples located at 2.85–3 V, 3.1–3.25 and 3.1–3.3 V in the **NHVO$_x$_*vac***, **KVO$_x$_*vac*** and **NaVO$_x$_HT_*vac*** samples, respectively, display peak separations between 150 and 200 mV, demonstrating a good reversibility of the Li insertion/extraction process. **NaVO$_x$_HT_*vac*** and **KVO$_x$_*vac*** also show cathodic peaks at 3.6 and 3.5 V, respectively, but the corresponding anodic counterparts appear shifted more than 500 mV at voltages higher than 4 V, suggesting a lower reversibility. Such an anodic process could be associated with partial Na^+ and K^+ migration and/or a possible oxidation of the electrolyte. Peaks above 3 V are not so well defined in the *_novac* electrodes, suggesting superposition of the electrochemical processes. Here, electrolyte decomposition could be discarded and the process at the highest voltage seems even more reversible in **NaVO$_x$_HT_*novac*** in accordance with the 3.6–3.75 V cathodic-anodic couple. Therefore, the vacuum-drying process could involve partial migration of the alkali ions in **NaVO$_x$_HT_*vac*** and **KVO$_x$_*vac***, electrolyte decomposition, and a decrease in the intercalation rate deduced by the gradual change in the shape of the CV curves.

The compounds are mixed valence systems that could be oxidized to +5 by charging the cell. Indeed, *_novac* electrodes were charged up to 4.5 V, showing first charge capacities of 39 mA h g^{-1} for **KVO$_x$** and **NHVO$_x$** and 66 mA h g^{-1} for **NaVO$_x$_HT** (Fig. S6†). Alkaline ions are arranged and supposed to act as "pillars" between the vanadium oxide layers stabilizing the structure during lithium ion intercalation and de-intercalation,[14,15] although a part of them could be extracted during the first charge.[64] Interestingly, *_vac* electrodes were not able to increase the potential above 4.0 V at 15 mA g^{-1} in the first charge forcing the measure to abort. In order to compare the behavior of the active materials dried in both conditions, all electrodes were previously discharged up to 1.5 V and then cycled between 1.5 and 4.5 V (*vs.* Li/Li$^+$). Fig. S7† shows the first galvanostatic charge–discharge profile of the electrodes at 15 mA g^{-1}. Discharge curves exhibit several regions according to the changes in slope: (a) I, from 3.9 V to 3.2–3.0 V, corresponding to 9–15% of the total discharge capacity, (b) II, from 3.2–3.0 V to 2.7–2.6 V, accounting for 15–20%, (c) III, from 2.7–2.6 V to 1.8–1.7 V is constituted by a two-step insertion of Li^+ in the host matrix and represents the main cathodic process delivering 55–60% of the discharge capacity, and (d) IV, from 1.8–1.7 V to 1.5 V which varies from 6 to 17% of the capacity depending on the sample. Segments I to III are consistent with the voltages and intensities found in the CV tests. Segment IV corresponding to an extra capacity below 1.8 V may be ascribed to either partial V^{4+} reduction to V^{3+} or the surface storage of Li^+.[65] **NaVO$_x$_HT_*vac*** and **KVO$_x$_*vac*** electrodes deliver the highest initial capacities, being 316 and 300 mA h g^{-1}, respectively, corresponding to the insertion of 2.34 and 2.17 Li/f.u. reaching an average vanadium oxidation state of 3.66+ and 3.74+, respectively. The amount of Li^+ ions inserted into the host lattices is slightly higher than the values reported in a similar material with the formula $Na_{0.32}V_2O_5{\cdot}0.01H_2O$.[66] In the case of **NHVO$_x$_*vac***, the highest discharge capacity recorded is 252 mA h g^{-1} or 1.8 Li/f.u. On the contrary, *_novac* electrodes display more moderate

capacity values, which are 251 mA h g^{-1} for **NaVO$_x$_HT**, 238 mA h g^{-1} for **NHVO$_x$**, and 229 mA h g^{-1} for **KVO$_x$**. These values correspond to 1.82 Li/f.u. for **NaVO$_x$_HT** and 1.7 Li/f.u. for **KVO$_x$** and **NHVO$_x$**, which implies an average vanadium oxidation state of around 3.92+ and 3.97+ at the end of the discharge. Therefore, a V^{3+}/V^{4+} state is expected for the *_vac* electrodes at 1.5 V, while the electrochemical role in the *_novac* electrodes is practically only played by the V^{4+}/V^{5+} redox couple.

The rate performances of the electrodes were also investigated (Fig. 7). The discharge profiles of the *_vac* electrodes exhibit steep falls with a dramatic reduction of their specific capacities as the current rate is increased, where the capacity decay is really noticeable in **NaVO$_x$_HT**. On the other hand, the main plateau around 2.5 V remains more robust in the *_novac* electrodes as the rate is increased. In fact, the **NaVO$_x$_HT_*novac*** electrode displays the best performance maintaining reversible discharge capacities over ten cycles at each C rate by delivering average capacities of 249, 229, 205, 187, 167 and 134 mA h g^{-1} at the current densities of 15, 30, 75, 150, 300 and 600 mA g^{-1}, respectively, with a notable coulombic efficiency of 98.8% after 60 cycles (Fig. S8†).

The highest discharge capacity values were normalized to 100% for each sample with the aim of emphasizing the differences in capacity retention as a function of current density (Fig. 8). Clearly, the electrodes dried without applying vacuum

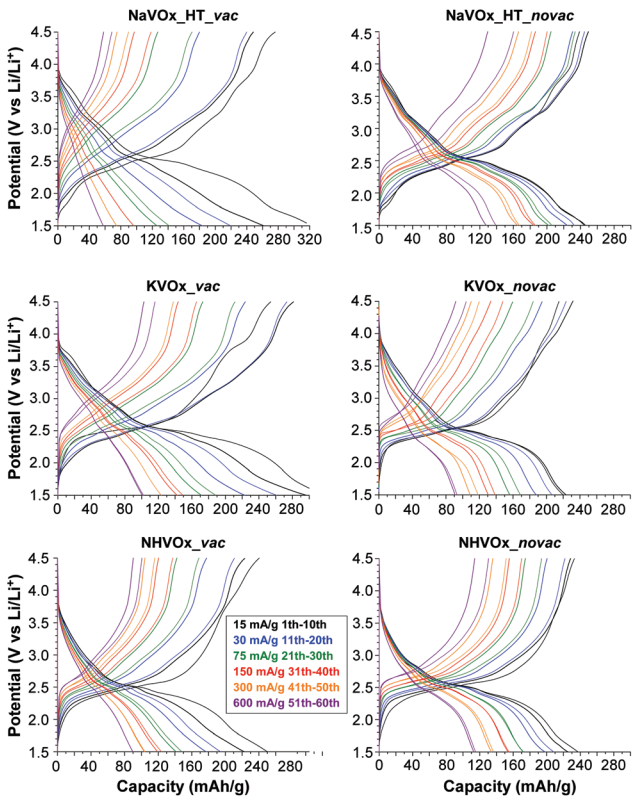

Fig. 7 Charge/discharge profiles of the *_vac* and *_novac* electrodes at different current densities, increasing from 15 to 600 mA g^{-1}.

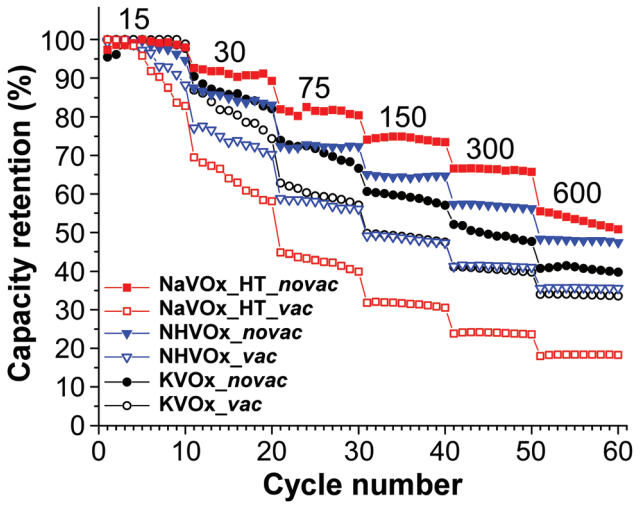

Fig. 8 Normalized discharge capacity retention of the *_vac* and *_novac* electrodes during the rate capability test from 15 to 600 mA g^{-1}.

exhibit better capacity retention at higher rates than the *_vac* homologues, being the response of the **NaVO$_x$_HT** samples worth mentioning. **NaVO$_x$_HT_*novac*** retained 92, 82, 75, 67 and 55% of the initial capacity (15 mA g^{-1}) when the current density was increased by 2, 5, 10, 20 and 40 times (30, 75, 150, 300 and 600 mA g^{-1}). Conversely, **NaVO$_x$_HT_*vac*** retained 69, 44, 32, 24 and 18% of the initial capacity with the same current density increase. Potassium and ammonium electrodes show intermediate trends but on the same lines as those observed for the sodium electrodes.

Given this circumstance, the cycling stability at high rates is expected to be ascribed to the disorder degree of the layered structures after drying under vacuum conditions; the higher the disorder degree, the lower the capacity retention under cycling at higher rates.

An *in situ* XRD experiment was performed in order to elucidate the structural mechanism upon electrochemical cycling of the phases. Fig. 9 shows a 2D plot of evolution of the XRD patterns of **KVO$_x$_*novac*** during the first two (dis)charge cycles and the corresponding voltage *vs.* time curve. *A priori*, the absence of new peaks during cycling suggests a solid solution mechanism instead of a two-phase reaction. The evolution of the cell parameter *c* is represented by the (00l) Bragg diffraction peaks, namely (002), (004) and (005). It was not possible to perform a sequential pattern matching because of the bad signal-to-noise ratio of the less intense reflections and the presence of artifacts (Al foil...) that overlap with **KVO$_x$** peaks. Therefore, (004) reflection was examined more deeply as it is the only one isolated during the whole cycling. A peak fit with FullProf was used to determine the evolution of its position and intensity (Fig. S9†). The (004) peak position is found to shift towards higher angles upon discharging concomitant to a decrease of the peak intensity. Such behavior is reversed during charging, indicating a decrease/increase of parameter *c* upon the insertion/extraction of Li^+. The analysis of the (00l)

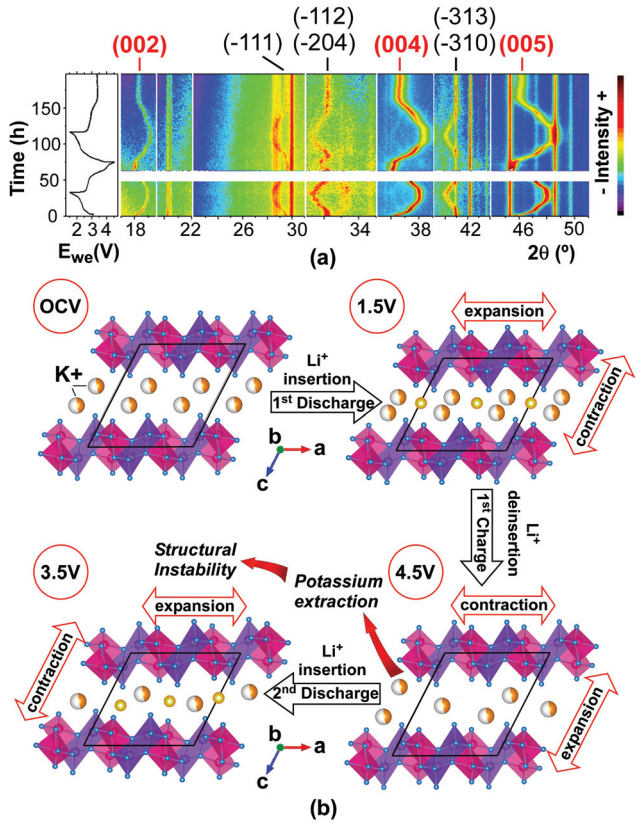

Fig. 9 (a) 2D plot of the *in situ* XRD experiment comprising the first two cycles and the corresponding voltage *vs.* time curve for KVO_x*_novac*. The colour level indicates the relative intensity of the peaks. Straight reflection lines invariant during the whole cycling represent artifacts of the cell. The horizontal blank space is a gap of 15 h due to a diffractometer failure. (b) Scheme of the possible structural mechanism upon electrochemical cycling at very low current density.

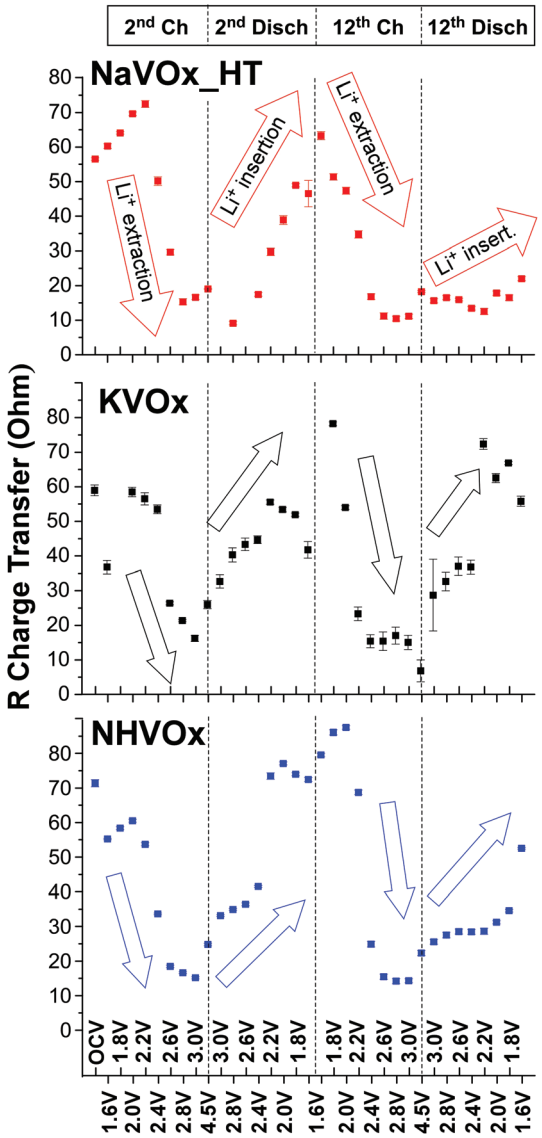

Fig. 10 Charge transfer resistance evolution during the 2nd and 12th charge/discharge cycles for the three vanadium oxide samples studied.

peaks, including the (001) main line of the *ex situ* XRD patterns of KVO_x collected at various (dis)charging depths in Li half-cells, reinforces the observed mechanism (Fig. S10†). As can be observed with the naked eye in Fig. 10, the parameters *a* and *b* would be experiencing an opposite structural response, that is, an expansion/contraction upon the insertion/extraction of Li^+.

A similar structural response was recently reported for a layered nickel orthotellurate based cathode for K-ion batteries.[67] For KVO_x*_novac*, the expansion of parameter *c* upon Li^+ extraction would imply an enhancement in the electrostatic repulsion between the vanadium oxide sheets and *vice versa* during Li^+ insertion. In parallel, the opposite behavior of parameters *a* and *b* concerning intra-slab effects could be related to the variations on the vanadium radius upon the oxidation/reduction process. In detail, an analysis of the patterns recorded at the limiting voltages, 1.5 V and 4.5 V, of the *in situ* XRD experiment reveals peak broadening (Fig. S11†). The most plausible hypothesis to explain the peak broadening arises from a disordering process resulting in microdomains with different interslab distances. Given that the *in situ* XRD experiment is carried out at a very low current density of 6 mA g^{-1}, a possible migration of the potassium host ions was speculated. Hence, for gaining a deeper insight into the phase evolution process of the KVO_x electrode, a Li half-cell was charged at 6 mA g^{-1} from OCV. Fig. S12† shows a charge capacity of 49 mA g^{-1} up to 4.35 V, where a flat plateau is revealed gaining an extra capacity of around 57 mA h g^{-1} up to 4.5 V, which confirms the potassium extraction at 6 mA g^{-1} resulting in a very fast capacity fading. Such extra capacity was not accessible when the cell was cycled at slightly higher current densities of 15 mA g^{-1} (Fig. S6†). The scheme of the structural degradation mechanism interpreted from the *in situ* XRD experiment is proposed in Fig. 10b.

To gain a deeper understanding of the electrochemical behaviour of *_novac* electrodes, electrochemical impedance spectroscopy (EIS) was performed during the second and

twelfth charge–discharge cycles at 75 mA g^{-1} (Fig. S13†). The EIS spectra of all phases at different representative voltages are illustrated in Fig. S14.† A model with 4 elements was used to fit the spectra for all samples; 3 RC elements and a Warburg diffusion element. In some cases, the diffusion process was not completely observed due to the very low frequency needed; therefore, it had to be modeled with a fourth RC element (Fig. S15†).

The high frequency region is consistent with resistance due to the surface film or contact resistance with the current collector, the middle frequency region describes the charge transfer process and the low frequency (sloping line) corresponds to the Li^+ solid state diffusion within the vanadium oxides. After the fitting all resistances were extracted and compared. Constant values or little variations were found in all cases, except for the charge transfer resistance (R_{CT}) in the three vanadium oxides (Fig. 10).

During charge transfer, R_{CT} tends to decrease while Li^+ is extracted from the material. Upon discharge, when Li^+ is inserted in the vanadium oxide structure, the charge transfer resistance increases. This is consistent with the interslab distance changes described in Fig. 9; as Li^+ is removed, the interslab distance increases due to electrostatic repulsion, facilitating further Li^+ extraction. The opposite trend is observed on Li^+ insertion. The fact that R_{CT} fluctuates following the same trend and showing similar maxima and minima for all samples is an indicator of the structural origin of this behaviour, which is independent of the pillaring ion (Na^+, K^+ or NH_4^+).

An interesting difference observed in the R_{CT} variations is found at the voltage where the plateau occurs, around 2.2–2.4 V. **KVO$_x$** and **NHVO$_x$** show sudden jumps in R_{CT} values from 2.4 to 2.2 V on charge and *vice versa*, from 2.2 to 2.4 V, on discharge. This phenomenon could be related to the structural changes that took place in the solid solution reaction mechanism. In fact, both the (004) and (005) peaks of **KVO$_x$** show a change in the shift rate at around 2.2–2.4 V upon charge and discharge (Fig. S11†). On the contrary, **NaVO$_x$_HT** does not exhibit such a sudden change of R_{CT} around the plateau, instead, the transition is more progressive. This could indicate smoother structural changes in the case of **NaVO$_x$_HT** and could possibly explain its superior electrochemical behaviour. Supporting this fact, the R_{CT} of **NaVO$_x$_HT** describes a less pronounced increase of its values during the Li^+ uptake in the discharge process of the 12th cycle reaching a value of 22 ohms at 1.6 V. **KVO$_x$** and **NHVO$_x$**, conversely, display larger values of 56 and 53 ohms, respectively, at the end of the discharge. Further experiments are needed to fully understand the correlations observed between the structural changes and charge transfer phenomena in these types of vanadium oxides.

Conclusions

Three mixed valency vanadium oxides with double layered delta type structures were synthesized *via* a single hydrothermal process. The interlayer spacing of the structures is modulated by the water content and the alkali (Na^+, K^+) and ammonium ions which display distinctive arrangements in their corresponding structures. According to XPS, an unusually high V^{4+} content was found in the V_2O_5 based matrices which must be due to the combination of a V^{4+} salt and a reducing agent during hydrothermal treatment. The monitoring of the V^{4+} EPR signal over time points to some metastability when the phases are exposed to air. The thermal behavior of the phases is conditioned by the nature of the crystallization of water molecules. For instance, **NaVO$_x$** undergoes a sudden structural transformation due to the loss of weakly hydrogen-bonded water molecules below 100 °C and **KVO$_x$** displays the highest thermal stability limit due to the presence of protonated water molecules. The electrochemical properties of the phases are highly dependent on the vacuum-drying process of the electrodes. CV curves demonstrated excellent electrochemical reversibility and superior cycling stability for the electrodes just dried at 100 °C. However, under a vacuum drying treatment, the electrodes suffer more capacity fading and possible partial migration of the alkali ions in **NaVO$_x$** and **KVO$_x$**. Rate capability also revealed better capacity retention for the electrodes treated without drying, where the **NaVO$_x$_HT_*novac*** electrode showed the best electrochemical performance. Alkali and ammonium ions are supposed to act as efficient pillars between bilayers to yield a stable interlayer contraction/expansion during lithium insertion/extraction. Such a role as structural stabilizers during cycling is compromised by an inadequate drying treatment of the electrodes giving rise to rapid capacity fading. The application of very low current densities during Li^+ cycling also triggers K^+ complete extraction in **KVO$_x$** at high voltages inducing the collapse of the V–O slabs.

Hence, the evaluation of the phases as intercalation-electrode materials for LiBs deserves further studies in structural and cycling stability testing, redefining a stable potential window to avoid irreversible reactions and evaluating the optimal procedure for the manufacture of electrodes. Furthermore, our findings might also open up possibilities to discover new applications for the archetypes presented here. The possibility of extracting alkaline ions that act as structural stabilizers against the insertion/extraction of Li^+ could be seen as the advantage of the material to be used, for instance, as the next generation high voltage cathode materials for potassium ion batteries.[68–71]

Conflicts of interest

There are no conflicts to declare.

Acknowledgements

J. O. and J. L. wish to thank the Millennium Nucleus Multimat for funding. J-L. G. C., M. J. and M. C. C. thank the Spanish Ministerio de Ciencia, Innovación y Universidades (MINECO) for funding through the ENE2016-81020-R project.

Notes and references

1 M. Schindler, F. C. Hawthorne and W. H. Baur, *Chem. Mater.*, 2000, **12**, 1248.
2 N. A. Chernova, M. Roppolo, A. C. Dillon and M. S. Whittingham, *J. Mater. Chem.*, 2009, **19**, 2526.
3 H. T. Tan, X. Rui, W. Sun, Q. Yan and T. M. Lim, *Nanoscale*, 2015, **7**, 14595.
4 M. S. Whittingham, Y. Song, S. Lutta, P. Y. Zavalij and N. A. Chernova, *J. Mater. Chem.*, 2005, **15**, 3362.
5 H. A. Wriedt, *Bull. Alloy Phase Diagrams*, 1989, **10**, 271.
6 D. A. Davydov and A. A. Rempel, *Inorg. Mater.*, 2009, **45**, 47.
7 S. H. Bae, S. Lee, H. Koo, L. Lin, B. H. Jo, C. Park and Z. L. Wang, *Adv. Mater.*, 2013, **25**, 5098.
8 T. S. Kasırga, D. Sun, J. H. Park, J. M. Coy, Z. Fei, X. Xu and D. H. Cobden, *Nat. Nanotechnol.*, 2012, **7**, 723.
9 M. S. Whittingham, *Chem. Rev.*, 2004, **104**, 4271.
10 Y. Lu, J. Wu, J. Liu, M. Lei, S. Tang, P. Lu, L. Yang, H. Yang and Q. Yang, *ACS Appl. Mater. Interfaces*, 2015, **7**, 17433.
11 S.-S. Cao, J.-F. Huang, H.-B. Ouyang, L.-Y. Cao, J.-Y. Li and J.-P. Wu, *Mater. Lett.*, 2014, **126**, 20.
12 H. Wang, K. Huang, S. Liu, C. Huang, W. Wang and Y. Ren, *J. Power Sources*, 2011, **196**, 788.
13 H. He, X. Zeng, H. Wang, N. Chen, D. Sun, Y. Tang, X. Huang and Y. Pana, *J. Electrochem. Soc.*, 2015, **162**(1), A39.
14 Y. Zhao, C. Han, J. Yang, J. Su, X. Xu, S. Li, L. Xu, R. Fang, H. Jiang, X. Zou, B. Song, L. Mai and Q. Zhang, *Nano Lett.*, 2015, **15**, 2180.
15 J. Meng, Z. Liu, C. Niu, X. Xu, X. Liu, G. Zhang, X. Wang, M. Huang, Y. Yu and L. Mai, *J. Mater. Chem. A*, 2016, **4**, 4893.
16 J. Galy, *J. Solid State Chem.*, 1992, **100**, 229.
17 P. M. Marley, G. A. Horrocks, K. E. Pelcher and S. Banerjee, *Chem. Commun.*, 2015, **51**, 5181.
18 C. J. Patridge, T.-L. Wu, C. Jaye, B. Ravel, E. S. Takeuchi, D. A. Fischer, G. Sambandamurthy and S. Banerjee, *Nano Lett.*, 2010, **10**, 2448.
19 P. Y. Zavalij and M. S. Whittingham, *Acta Crystallogr., Sect. B: Struct. Sci.*, 1999, **55**, 627.
20 H. Wang, K. Huang, C. Huang, S. Liu, Y. Ren and X. Huang, *J. Power Sources*, 2011, **196**, 5645.
21 Y. Ma, S. Ji, H. Zhou, S. Zhang, R. Li, J. Zhu, W. Li, H. Guo and P. Jin, *RSC Adv.*, 2015, **5**, 90888.
22 Y. Liu, M. Xu, B. Shen, Z. Xia, Y. Li, Y. Wu and Q. Li, *J. Mater Sci.*, 2018, **53**, 2045.
23 S. Sarkar, P. S. Veluri and S. Mitra, *Electrochim. Acta*, 2014, **132**, 448.
24 H. Fei, X. Liu, Y. Lin, M. Wei and J. Colloid, *Interface Sci.*, 2014, **428**, 73.
25 T. Sarkar, P. Kumar, M. D. Bharadwaj and U. Waghmare, *Phys. Chem. Chem. Phys.*, 2016, **18**, 9344.
26 A. Sarkar, S. Sarkar, T. Sarkar, P. Kumar, M. D. Bharadwaj and S. Mitra, *ACS Appl. Mater. Interfaces*, 2015, **7**, 17044.
27 A. Sarkar, S. Sarkar and S. Mitra, *J. Mater. Chem. A*, 2017, **5**, 24929.
28 Q. Chen, Q. Xia, Y. Xu, P. Wang and Q. Tan, *Mater. Lett.*, 2019, **247**, 178.
29 E. A. Esparcia Jr., M. S. Chae, J. D. Ocon and S.-T. Hong, *Chem. Mater.*, 2018, **30**, 3690.
30 B. Tang, J. Zhou, G. Fang, F. Liu, C. Zhu, C. Wang, A. Pan and S. Liang, *J. Mater. Chem. A*, 2019, **7**, 940.
31 G. Yang, T. Wei and C. Wang, *ACS Appl. Mater. Interfaces*, 2018, **10**, 35079.
32 T. N. Vo, H. Kim, J. Hur, W. Choi and T. Kim, *J. Mater. Chem. A*, 2018, **6**, 22645.
33 J. Lai, H. Zhu, X. Zhu, H. Koritala and Y. Wang, *ACS Appl. Energy Mater.*, 2019, **2**, 1988.
34 J. Shin, D. S. Choi, H. J. Lee, Y. Jung and J. W. Cho, *Adv. Energy Mater.*, 2019, **9**, 1900083.
35 D. Kundu, B. D. Adams, V. Duffort, S. H. Vajargah and L. F. Nazar, *Nat. Energy*, 2016, **1**(10), 16119.
36 Y. Oka, T. Yao, N. Yamamoto, Y. Ueda and A. Hayashi, *J. Solid State Chem.*, 1993, **105**, 271.
37 A. Altomare, C. Cuocci, C. Giacovazzo, A. Moliterni, R. Rizzi, N. Corriero and A. Falcicchio, *J. Appl. Crystallogr.*, 2013, **46**, 1231.
38 J. Rodriguez-Carvajal, *Phys. B*, 1993, **192**, 55.
39 P. Thompson, D. E. Cox and J. B. Hastings, *J. Appl. Crystallogr.*, 1987, **20**, 79.
40 N. C. Popa, *J. Appl. Crystallogr.*, 1998, **31**, 176.
41 M. Casas-Cabanas, M. R. Palacín and J. Rodriguez-Carvajal, *Powder Diffr.*, 2005, **20**, 334.
42 Y. Oka, T. Yao and N. Yamamoto, *Nippon Seramikkusu Kyokai Gakujutsu Ronbunshi*, 1990, **98**, 1365.
43 T. Yao, Y. Oka and N. Yamamoto, *J. Mater. Chem.*, 1992, **2**(3), 331.
44 Y. Oka, T. Yao and N. Yamamoto, *J. Mater. Chem.*, 1995, **5**, 1423.
45 T. Yao, Y. Oka and N. Yamamoto, *J. Mater. Chem.*, 1996, **6**, 1195.
46 T. Chirayil, P. Y. Zavalij and M. S. Whittingham, *Chem. Mater.*, 1998, **10**, 2629.
47 F. Zhang, P. Y. Zavalij and M. S. Whittingham, *Mater. Res. Bull.*, 1997, **32**(6), 701.
48 F. Zhang and M. S. Whittingham, *Electrochem. Commun.*, 2000, **2**, 69.
49 Y. Oka, T. Yao and N. Yamamoto, *J. Solid State Chem.*, 1997, **132**, 323.
50 H. H. Kristoffersen and H. Metiu, *J. Phys. Chem. C*, 2016, **120**, 3986.
51 V. Petkov, P. N. Trikalitis, E. S. Bozin, S. J. L. Billinge, T. Vogt and M. G. Kanatzidis, *J. Am. Chem. Soc.*, 2002, **124**, 10157.
52 P. N. Trikalitis, V. Petkov and M. G. Kanatzidis, *Chem. Mater.*, 2003, **15**, 3337.
53 M. Najdoski, V. Kolevac and A. Sameta, *Dalton Trans.*, 2014, **43**, 12536.
54 G. T. Chandrappa, P. Chithaiah, S. Ashoka and J. Livage, *Inorg. Chem.*, 2011, **50**, 7421.
55 S. Bacha, A. Boudaoud, N. Emery, R. Baddour-Hadjean and J. P. Pereira-Ramos, *Electrochim. Acta*, 2014, **119**, 38.

56 R. Baddour-Hadjean, A. Boudaoud, S. Bach, N. Emery and J. P. Pereira-Ramos, *Inorg. Chem.*, 2014, **53**, 1764.
57 R. Baddour-Hadjean, J. P. Pereira-Ramos, C. Navone and M. Smirnov, *Chem. Mater.*, 2008, **20**, 1916.
58 R. Baddour-Hadjean and J. P. Pereira-Ramos, *Chem. Rev.*, 2010, **110**, 1278.
59 V. K. Sharma, A. Wokaun and A. Baiker, *J. Phys. Chem.*, 1986, **90**, 2715.
60 A. Kahn, J. Livage and R. Collongues, *Phys. Status Solidi A*, 1974, **26**, 175.
61 O. R. Nascimento, C. J. Magon, L. V. S. Lopes, J. P. Donoso, E. Benavente, J. Paez, V. Lavayen, M. A. Santa Ana and G. Gonzalez, *J. Sol-Gel, Sci. Technol.*, 2008, **45**, 195.
62 C. J. Magon, J. F. Lima, J. P. Donoso, V. Lavayen, E. Benavente, D. Navas and G. Gonzalez, *J. Magn. Reson.*, 2012, **222**, 26.
63 V. A. Nikitina, S. M. Kuzovchikov, S. S. Fedotov, N. R. Khasanova, A. M. Abakumov and E. V. Antipov, *Electrochim. Acta*, 2017, **258**, 814.
64 D. Fang, Y. Cao, R. Liu, W. Xu, S. Liu, Z. Luo, C. Liang, X. Liu and C. Xiong, *Appl. Surf. Sci.*, 2016, **360**, 658.
65 J. Prado-Gonjal, B. Molero-Sánchez, D. Ávila-Brande, E. Morán, E. J, C. Pérez-Flores, A. Kuhn and F. García-Alvarado, *J. Power Sources*, 2013, **232**, 173.
66 C.-Y. Lee, A. C. Marschilok, A. Subramanian, K. J. Takeuchi and E. S. Takeuchi, *Phys. Chem. Chem. Phys.*, 2011, **13**, 18047.
67 T. Masese, K. Yoshii, Y. Yamaguchi, T. Okumura, Z.-D. Huang, M. Kato, K. Kubota, J. Furutani, Y. Orikasa, H. Senoh, H. Sakaebe and M. Shikano, *Nat. Commun.*, 2018, **9**, 3823.
68 K. Chihara, A. Katogi, K. Kubota and S. Komaba, *Chem. Commun.*, 2017, **53**, 5208.
69 J. Han, G.-N. Li, F. Liu, M. Wang, Y. Zhang, L. Hu, C. Dai and M. Xu, *Chem. Commun.*, 2017, **53**, 1805.
70 W. B. Park, S. C. Han, C. Park, S. U. Hong, U. Han, S. P. Singh, Y. H. Jung, D. Ahn, K.-S. Sohn and M. Pyo, *Adv. Energy Mater.*, 2017, **8**, 1703099.
71 T. Masese, K. Yoshii, M. Kato, K. Kubota, Z.-D. Huang, H. Senoh and M. Shikano, *Chem. Commun.*, 2019, **55**, 985.